# Measurement of aberrations of a solid elastic lens using a point-diffraction interferometer

**Agustin Santiago-Alvarado**
Universidad Tecnológica de la Mixteca
Carretera Acatlima Km 2.5
Huajuapan de León
Oaxaca, México 69000
E-mail: santiago@mixteco.utm.mx

**Sergio Vázquez-Montiel,** MEMBER SPIE
**Fermín-Salomón Granados-Agustín,** MEMBER SPIE
Instituto Nacional de Astrofísica
Óptica y Electrónica INAOE
Calle Luis Enrique Erro #1
Tonantzintla Puebla, México 72840

**Jorge González-García**
Universidad Tecnológica de la Mixteca
Carretera Acatlima Km 2.5
Huajuapan de León
Oaxaca, México 69000

**Esteban Rueda-Soriano,** MEMBER SPIE
Instituto Nacional de Astrofísica
Óptica y Electrónica INAOE
Calle Luis Enrique Erro #1
Tonantzintla Puebla, México 72840

**Manuel Campos-García**
Universidad Nacional Autónoma de México
Centro de Ciencias Aplicadas y Desarrollo Tecnológico
Apdo. Postal 70-186
México, México 04510

**Abstract.** There has been a considerable recent increase in the use of variable focal length lenses (VFLLs), especially as microlenses in photographic objectives, endoscopes, microscope objectives, etc. One distinguishing feature of these VFLLs is the presence of a mechanism whereby the shape of the lens and its geometrical parameters can be changed. A new type of variable focal length lens is introduced made from elastic material. It is placed inside a mechanical mount where radial forces can be applied to its perimeter. We also present the optomechanical design and the measurement of wavefront aberrations to the third and fifth order of a solid elastic lens (SEL). A point-diffraction interferometer is used as a wavefront sensor to test changes of the lens. Geometrical changes in the lens produce changes in the aberrations. Finally, the aberrations found in the SEL (without any application of stress) are compared with aberrations obtained by means of numerical ray trace. Some experimental results are also shown. 
[DOI: 10.1117/1.3522645]

Subject terms: elastic lens; aberrations; point-diffraction interferometer.

Paper 100030PRR received Jan. 14, 2010; revised manuscript received Oct. 19, 2010; accepted for publication Oct. 21, 2010; published online Dec. 10, 2010.

## 1 Introduction

Many optical systems in everyday use employ hard lenses made from glass or plastic, as is the case of photographic cameras, video cameras, microscopes, zoom systems, etc.[1] Focusing in these systems is done by moving some of the components. In human beings, focusing is done by changing the shape of the crystalline lens of the eye.[2]

A number of efforts have been made to design and manufacture lenses that change their focal length by replicating the way crystalline functions in the human eye, due to the possibility of making lighter, simpler, and more compact optical devices, as in the case of tunable focus lenses. Today, there is growing interest in variable focal length lenses and a number of different types can be found: for example, tunable liquid lenses composed of a cylindrical metallic mechanical mount with a compartment for two transparent elastic surfaces filled with gas or liquid. Modifying the quantity of medium within the mount causes the axial thickness and the curvature radii of the surfaces to change.[3,4] There are also microlenses made from a dielectric liquid medium that changes its focal length when an electric field is applied.[5] Other lenses change their refractive index to produce changes in their geometrical parameters.[6] Such tunable lenses require a relatively high voltage of approximately 100 V. Furthermore, the construction of a large-aperture electrowetting lens can be quite a complicated process,[7] or it may require an elaborate mechanical hydropneumatic system to produce focus tuning.[8,9]

A recent study in which we used liquid lenses with variable focal lengths, describes the design, manufacture, and the mechanical characterization of elastic membranes and components as well as their optical performance.[10,11] These elastic membranes were made from Sylgard 184 Silicone Elastomer.[12] In another paper, we described the optomechanical design, manufacturing process, and the type of image produced by a solid elastic lens (SEL) made from the same material.[13]

This paper describes the mechanical performance and aberrations found in a variable focal length lens (VFLL) of the SEL type when radial stress is applied on its perimeter to

0091-3286/2010/$25.00 © 2010 SPIE

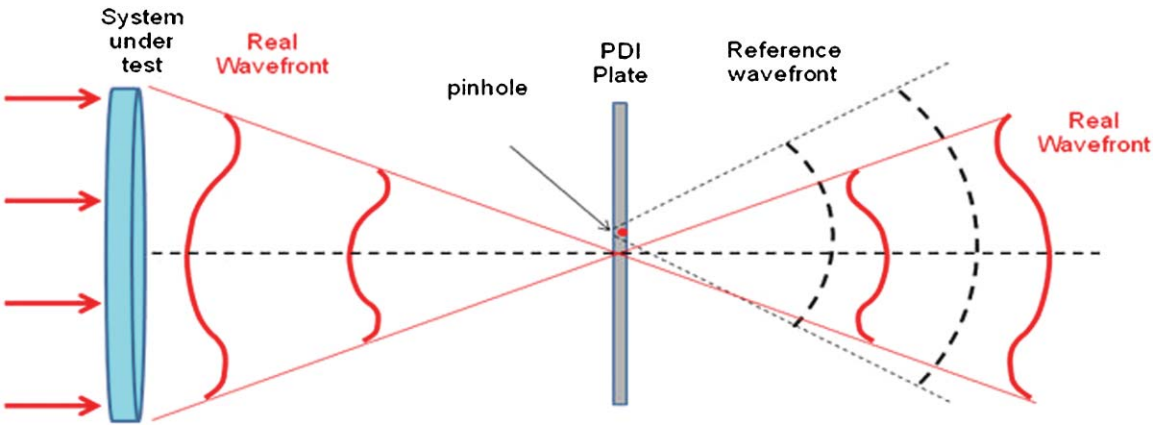


**Fig. 1** PDI operating principle.

produce a tunable focus lens. A point-diffraction interferometer (PDI) was used to measure the wavefront aberrations of the SEL. The technique employed is easy to set up because only a wavefront sensor is used.[14] The next section provides a description of the PDI test followed for an analysis of the design, construction, and performance of the SEL. Then we describe the process for evaluating the lens using an experimental setup to record and evaluation of interference patterns by means of an ApexWin$^{TM}$ commercial program (version 3.0.1); experimental results and conclusions are given at the end of the paper.

## 2 PDI

The PDI was proposed by Linik[15] in 1933 is a simple commonpath interferometer capable of directly measuring optical path differences (OPDs). The PDI is basically a two-beam interferometer in which a reference beam is generated by the diffraction from a small pinhole in a semitransparent coating and the light beam that passes through the region around the pinhole in the semitransparent coating. The portion of the light beam that passes through the region around the micro-orifice is reduced in intensity. Once these two light beams have passed through the substrate, they begin to interfere with one another and generate an interferogram[16–18] (see Fig. 1).

Fourier theory can be used to determine the resultant optical amplitude in the image plane of the system under test due to the effects of the PDI. A complete description of the theory can be founded in the literature.[14,19]

## 3 Solid Elastic Lens

A number of attempts have been made to design and manufacture lenses that change their focal length to mimic the behavior of crystalline lenses in the human eye. One such lens is the SEL, which can be deformed by applying radial forces on its edges. The SEL is a simple system composed of a mechanical mount that can apply radial forces by means of a system of cogs encrusted within the transparent elastic material which makes up the body of the lens (see Fig. 2).

The elastic material of the SEL is polydimethylsiloxane (PDMS) Sylgar 184 elastomer[12]; the PDMS allows deformations of the original shape of the lens, and recovers the original shape when the radial forces are withdrawn. The SEL (shown in Fig. 3) is constructed with a mechanical mount of aluminium, while the body of the lens is made of PDMS. A recently developed study gives a description of the design,

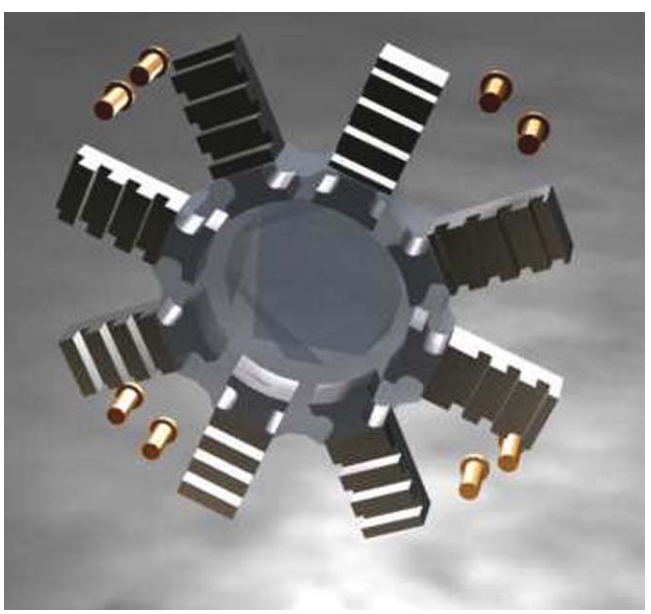

**Fig. 2** Mechanical system used to apply radial forces on the SEL.

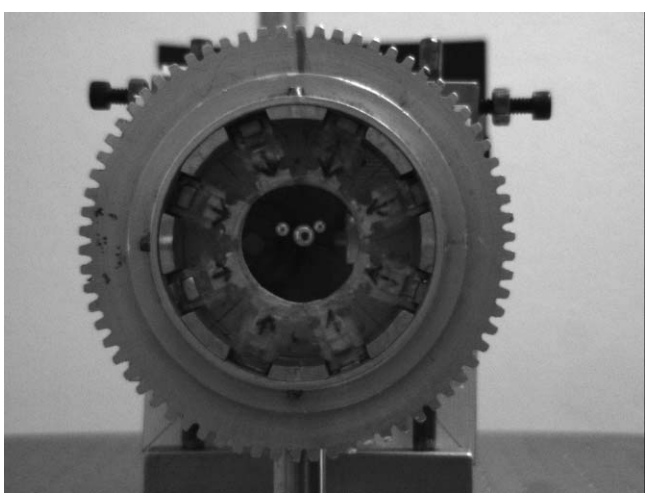

**Fig. 3** Front view of the SEL with a cogged disk for applying radial forces.


**Fig. 4** Setup of the PDI: (1) He-Ne laser, (2) expander, (3) pinhole, (4) diaphragm, (5) collimator lens, (6) SEL, (7) phase plate with pinhole for PDI test, and (8) CCD camera.

manufacture and mechanical performance[13,20,21] of the SEL, where the rotation of a toothed disk applies radial forces on the perimeter of the lens.

The geometrical parameters of the SEL were measured experimentally[13,20] (without applying radial forces), showing a focal length of 121 mm, a diameter of 30 mm, an $f$-number of 4.5, and a refraction index of 1.4157.

On the other hand, to measure the wavefront with the PDI method, the phase plate was fabricated using the mercury drop technique,[17] in which a circular orifice was made with a diameter of 14 $\mu$m on the phase plate (manufactured in INAOE with a transmittance of 1%).

## 4 Optical Performance of the SEL

An experimental setup was made to test the SEL (see Fig. 4), onto which a plane wavefront was directed, that is, an infinite point source on the axis was considered. Before applying a radial stress on the SEL, the minimum confusion spot generated by this was found (see Fig. 5; only the presence of spherical aberration would be expected). The spot was captured at a distance of 121 mm from the front vertex of the lens. Figure 5 (millimetrical sheet) shows that the size of the spot is about 1 mm in diameter. On the other hand, the axial and marginal thickness, diameter, and refraction index were measured experimentally, obtaining $t = 4.22$ mm, $e = 2$ mm, $d = 30$ mm, and $n = 1.4157$, respectively, and from these data the curvature radii of the biconvex lens were found with a value $r = 101.91$ mm (the diameter of the lens was 30 mm). For the manufacture of the lens, two spherical surface molds with an optical quality of $\pi/2$ were used; a PDMS mixture was deposited between them together with the jaws. After 7 days, the molds were removed and the lens embedded with the jaws was obtained. The axial and marginal thickness of the SEL were experimentally measured using a Mitutoyo micrometer with a precision of 1 $\mu$m. The curvature radii of the mold surfaces were also experimentally measured with a Howard Strasbaugh Inc. trademark mechanical spherometer. Furthermore, with the measured parameters and using Eqs. (1) and (2), the radii curvature of the lens surfaces were calculated to verify that both had the same value, using

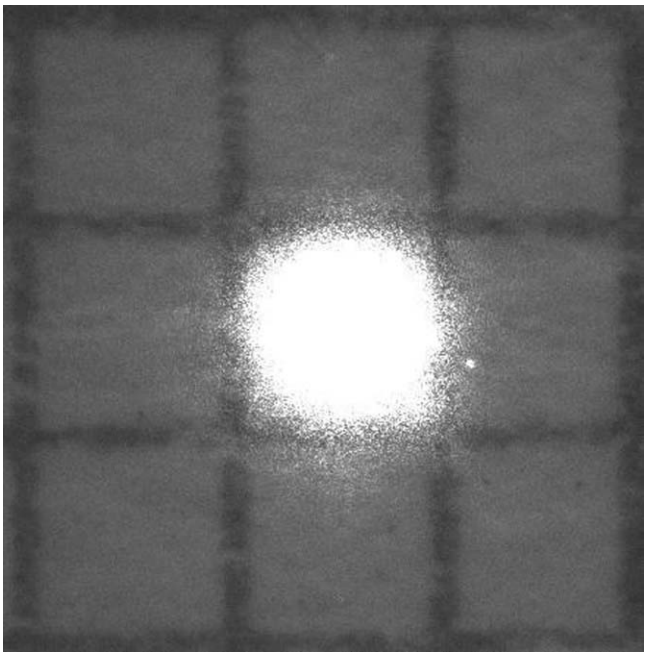

**Fig. 5** Minimum confusion spot generated by the SEL.

$$\varepsilon_p = 2Z + \varepsilon_m, \tag{1}$$

$$Z = R - (R^2 - \rho^2)^{1/2}, \tag{2}$$

where $R$ is the radius of curvature, $\rho$ is the lens semidiameter, $Z$ is the sagitta, $\varepsilon_m$ is the marginal thickness, and $\varepsilon_p$ is the paraxial thickness.

These parameters were put into the OSLO$^{TM}$ program[22] and a ray trace was performed for the lens. Figure 6 shows the minimum confusion spot produced by the program at a distance of 121.82 mm from the surface vertex, and a spot size of approximately 1 mm in diameter.

To change the focal length (or the shape) of the SEL, stress was applied by the radial movement of the system of encrusted cogs. This was done by a cogwheel making linear displacements of the encrusted cogs since these follow a helicoidal trajectory. Here, the maximum radial displacement

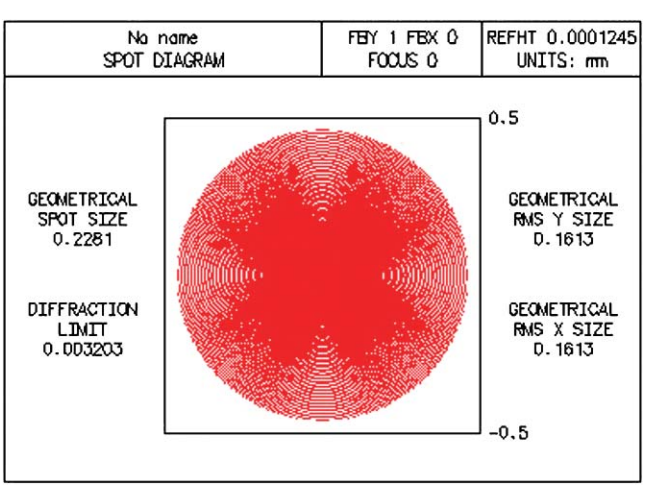


**Fig. 6** Spot diagram of the SEL generated with OSLO.

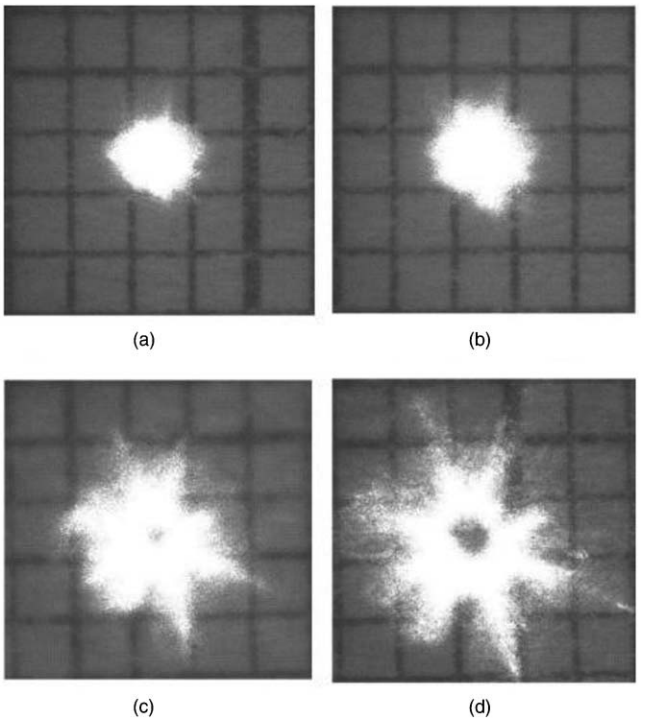


**Fig. 7** Spot diagrams generated by the SEL as the cogwheel rotates (a) 30.86 deg, (b) 41.14 deg, (c) 72 deg, and (d) 97.71 deg.

of the encrusted cogs was 3.2 mm at the end of a complete round, or after displacing the 70 teeth (the angular displacement of a tooth is equivalent to 5.14 deg); Fig. 7 shows the spot diagrams generated by the SEL when the cogwheel rotates: Fig. 7(a) 30.86 deg, Fig. 7(b) 41.14 deg, Fig. 7(c) 72 deg and Fig. 7(d) 97.71 deg. The position of the image plane in relation to the SEL was kept constant at 121 mm. An angular displacement of 5.14 deg produces a radial displacement of 45 $\mu$m in the encrusted cogs on the lens.

Figure 7 shows that when radial stress is applied, the shape of the spot changes irregularly, thereby revealing that there

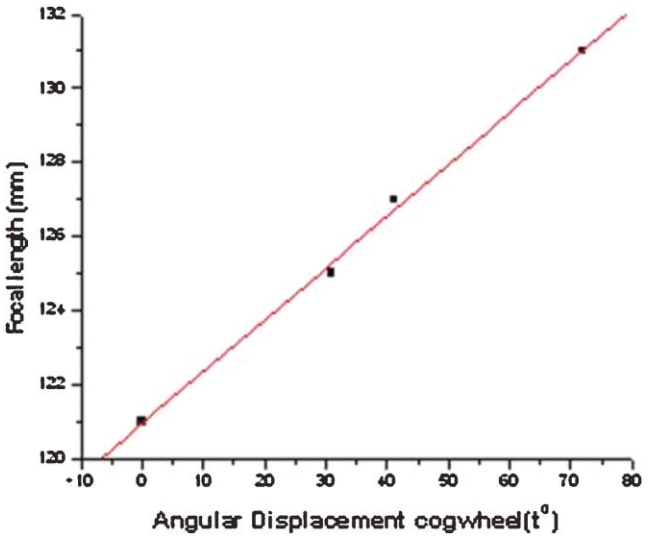


**Fig. 8** Graph of back focal length against the angular displacement of the cogwheel.

is greater displacement in the lens zones where the cogs are encrusted, and that some of them apply greater stress than others. As a result of this, trying to measure the shape of lens surfaces using mechanical methods can be quite difficult, and therefore only aberrations with the PDI technique were taken. To correct these problems, greater attention must be paid at the process of curing the PDMS mix on the lens mold. To verify that the encrusted cogs do not move and leave a space without mix, this ensures that all the encrusted cogs exert the same force on the lens when the cogwheel rotates. On the other hand, care must be taken to ensure that no air gets trapped inside the mold when the PDMS mixture is added so as to avoid bubbles being formed in the body of the lens.

To improve the shape of the image obtained, the number of cogs must be increased to produce displacements in a greater number of zones of the surface, which are evenly spaced on the perimeter of the surface. In view of all this, it is clear

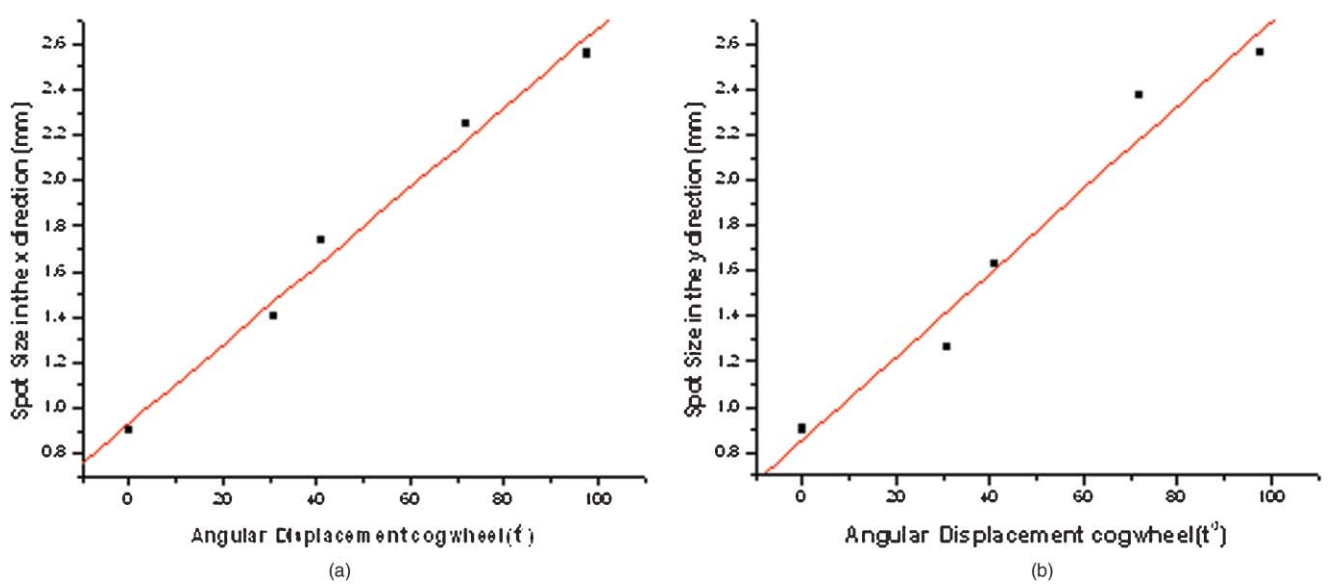


**Fig. 9** Graphs of the angular displacements of cogwheel against the spot size (a) in the *x* direction and (b) in the *y* direction.

that, as well as the spherical aberration, other aberrations are found in the formed images.

To test the SEL focus for each of the angular displacements generated, the image plane was moved to find the minimum confusion spot and the focal length was measured. As the applied stress increased (by rotating the cogwheel and thereby displacing the teeth) the distance at which the minimum confusion spot was formed also increased. The graph in Fig. 8 was made with the data measured and the experimentally obtained images. In this graph, the back focal length is plotted as a function of the stress applied by the encrusted cogs when the cogwheel was rotated to a particular certain angle (the angular displacement of a tooth is equivalent to 5.14 deg). Hence, the displacement generated by the angle of the rotation of the cogwheel is on the horizontal axis; the back focal length obtained is on the vertical axis (see Fig. 8). By making a least-squares fit to the data measured, the following relationship was obtained for the back focal length as a function of the angular displacement:

$$BFL = 0.14t + 120.96, \tag{3}$$

where $t$ is the angle rotated. The focal length is given in millimeters. The resulting standard deviation is 0.28 mm.

Furthermore, the minimum confusion spot sizes are plotted as a function of the stress applied by rotating the cogwheel (see Fig. 9). The following relationships were obtained by fitting with least squares:

$$R_x = 0.089x + 0.93, \tag{4}$$

and

$$R_y = 0.095x + 0.852, \tag{5}$$

where $x$ is the angular displacement of the mount, and $R_x$ and $R_y$ are the diameters of the spots in the $x$ and $y$ directions, respectively. The standard deviation obtained for each fit was 0.087 mm for $X$ and 0.156 mm for $Y$. As we can see in Fig. 9, the stress produced by the encrusted cogs on the lens is not uniform, and consequently the size of the spot is not symmetrical.

## 5 Recording and Evaluating SEL Interferograms

To measure the wavefront aberrations found in this type of lens, interference patterns were generated using a PDI, of which a schematic model is shown in Fig. 10.

Here a point source and a collimated lens were used to generate a plane wavefront. The generated plane wave passed through the SEL and we placed the phase plate at the focal plane of the lens. Afterward, a CCD camera was used to capture the interference pattern, which was processed using[23] ApexWin$^{TM}$ version 3.1, which is commercial software that is no longer available due to company closure.

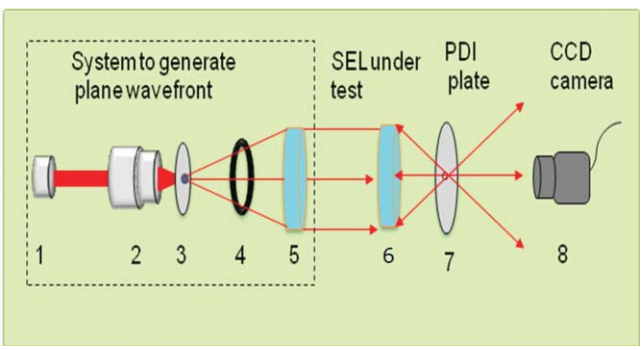


**Fig. 10** Schematic model of PDI: (1) He-Ne laser, (2) expander, (3) pinhole, (4) diaphragm, (5) collimator lens, (6) SEL, (7) phase plate with pinhole for PDI test, and (8) CCD camera.

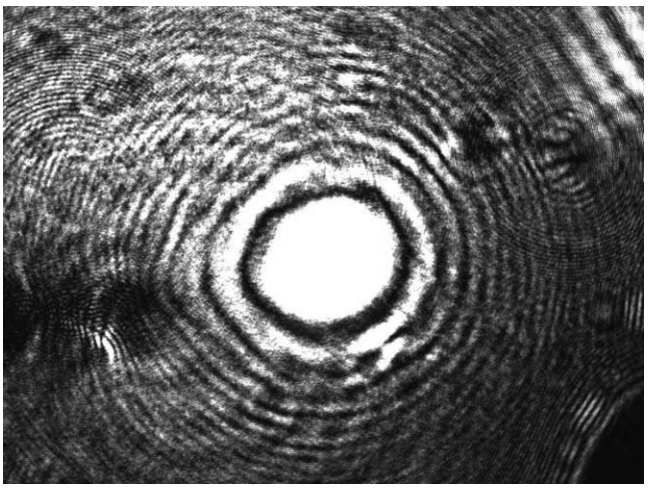

**Fig. 11** Interferogram of SEL without applying radial forces.

An interferogram was obtained of the SEL without applying radial forces (see Fig. 11), and it was analyzed and evaluated with ApexWin$^{TM}$. Results of the evaluation are shown in Table 1. To clarify, we changed the position of the pinhole, and this movement was taken as defocus, or tilt, in the aberrations obtained in the evaluation, and should not be considered part of the defects of the lens. Finally, using the Zernike coefficients obtained by the ApexWin$^{TM}$ program, we generated the synthetic interferogram with the same program, as shown in Fig. 12. The ApexWin$^{TM}$ program calculates the Zernike coefficient using the orthogonalization method of Gram-Schmidt.[24]

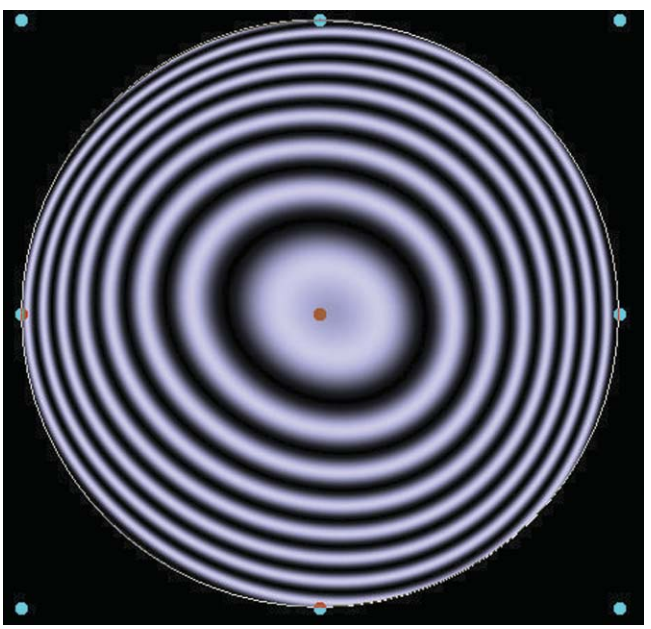

**Fig. 12** Synthetic interferogram generated with ApexWin$^{TM}$.

**Table 1** Aberrations found in the SEL without applying radial forces (evaluated with ApexWin$^{TM}$).

| | Zernike Data | PDI within the Focus | 16 Terms |
|---|---|---|---|
| Third order aberrations in wavelengths | | ($\lambda = 632.8$ nm) | |
| Spherical | 0.13 | Piston | 0 |
| Coma in *Y* | 0.095 | Focus | 1.95 |
| Coma in *X* | 0.01 | Tilt in *X* | 0.0 |
| Stigmatism 45 deg | 0.105 | Tilt in *Y* | 0.0 |
| Stigmatism 0 deg | −0.14 | | |
| Fifth order aberrations in waves ($\lambda = 632.8$ nm) | | | |
| Spherical | 0.005 | | |
| Coma in *Y* | 0.045 | 0 deg Tri | −0.03 |
| Coma in *X* | −0.06 | 30 deg Tri | −0.15 |
| Stigmatism 45 deg | −0.11 | | |
| Stigmatism 0 deg | 0.075 | | |

The generated interference pattern shown in Fig. 12 has a root mean square (rms) of 0.12 λ and a peak to valley of 3.04 λ, using an He-Ne laser with a wavelength of 632.8 nm.

On the other hand, to measure wavefront aberrations present in this type of lens when radial stress was applied, interference patterns were generated with the help of the PDI (see Fig. 13). Each interferogram was evaluated with the ApexWin$^{TM}$ program. The interferogram evaluation was carried out as follows: first, we displayed the interferogram in the interface program, then we fitted and gave order to the fringes on the interferogram, next we selected the Zernike coefficient number that the program was going to take to do the fit. After that, we took the same Zernike coefficients and generated the synthetic interferogram (simulated interferogram) with the same program. Finally, these interferograms were compared to reach a high correlation. If the correlation is low, other Zernike coefficients are taken and the process is repeated. Results of the evaluations of the aberrations are shown in the graph of Fig. 14 and in Table 2.

As we can see in Table 2, the aberrations (found in the SEL when radial stress is applied) change in a nonlinear fashion (see the plot in Fig. 14). This is due to the small number of jaws employed and problems in the curing of the lens since not all the jaws applied the same radial stress on the lens.

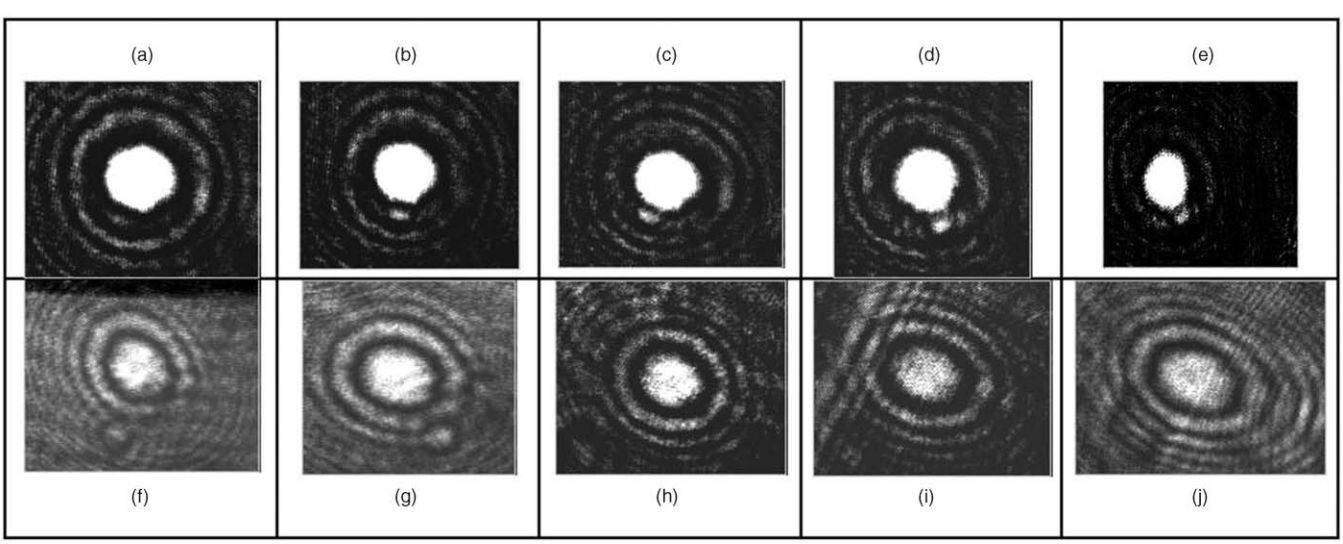


**Fig. 13** Interferograms of SEL generated with the PDI technique as the cogwheel rotates an angle of (a) 0, (b) 10.29, (c) 20.57, (d) 30.86, (e) 41.14, (f) 51.43, (g) 56.57, (h) 61.71, (i) 66.86, and (j) 72.00 deg, respectively.

**Table 2** Data obtained from the evaluation and analysis of the patterns in Fig. 13.

| Tooth Rotations | Piston | Focus | *Y* Tilt | *X* Tilt | Spherical | *Y* Coma | *X* Coma | 45-deg Astig. | 0-deg Astig. |
|---|---|---|---|---|---|---|---|---|---|
| 0 | 1.675 | 1.275 | 0.03 | −0.005 | 0.125 | −0.055 | 0.02 | −0.055 | −0.185 |
| 2 | 1.875 | 1.01 | −0.01 | 0.065 | −0.025 | −0.04 | −0.01 | −0.025 | −0.185 |
| 4 | 1.47 | 1.115 | −0.16 | 0.055 | −0.05 | 0.15 | −0.065 | −0.1 | −0.19 |
| 6 | 1.29 | 0.985 | −0.005 | 0.145 | 0.085 | −0.035 | 0.085 | −0.16 | 0.01 |
| 8 | 1.66 | 0.805 | 0.08 | 0.035 | −0.02 | 0.04 | 0.045 | −0.155 | −0.1 |
| 10 | 2.17 | 1.695 | 0 | 0.295 | −0.045 | −0.065 | 0.015 | −0.55 | −0.305 |
| 11 | 1.53 | 1.155 | −0.045 | 0.325 | −0.205 | −0.02 | −0.13 | −0.345 | −0.16 |
| 12 | 1.88 | 1.735 | −0.03 | 0.06 | 0.065 | 0.115 | −0.16 | −0.465 | −0.815 |
| 13 | 1.45 | 0.545 | −0.01 | 0.03 | −0.635 | −0.19 | −0.055 | −0.195 | −0.015 |
| 14 | 2.55 | 2.36 | −0.18 | 0.145 | −0.085 | 0.015 | −0.075 | −0.95 | −1.35 |

### 5.1 *Simulated Interferogram of SEL*

To simplify, we consider the case where radial forces are not present on the SEL. Then, once the SEL interference patterns have been obtained with the PDI method and evaluated with ApexWin™, the Zernike aberration coefficients were found for the third and fifth orders without applying radial forces (see Table 1). Next, the experimental geometrical parameters (Sec. 4) of the SEL were introduced into OSLO™ to simulate the interference pattern and obtain the Zernike aberration coefficients, where we consider a 1.45 defocus on the image plane the same as in the experimental case. The results are shown in Table 3 and in Fig. 15. The rms value in the OPD turned out to be 1.75 with a peak to valley of 6.03. A comparison between the simulated pattern and the real pattern reveals a similarity in the shape, and also shows irregularities in the real patterns due to problems that arose while manufacturing the lens, as can be seen in the SEL in Fig. 3. As the mixture was being passed from the mold to perform the curing process, some air bubbles could not be removed and were left in the lens.

Furthermore, irregularities were found on one of the surfaces of the lens. This problem arose when the SEL was being removed from the mold, and also with some particles of dust sticking to the surface. This can be seen in the lack of symmetry in the interference patterns. In spite of all this, there is a great deal of similarity between the real pattern and the one simulated with OSLO™, as can be seen in Figs. 12 and 15. The rms found in each one of these patterns is different because the real interference pattern is for only a part of the lens, whereas the simulated pattern is of the entire surface. As a result, errors in the peak to valley in one of them is double that of the other. The reason for this is because at the time when the interference pattern in the arrangement of the PDI was being captured, a defocus was introduced. This could have brought about the slight difference from the one obtained with ApexWin™. Furthermore, in the simulated interferogram, there are none of the errors that arose during the manufacture and measurement of the geometrical parameters of the lens, or when performing the interferometric evaluation (imperfections in the pinhole of the PDI).

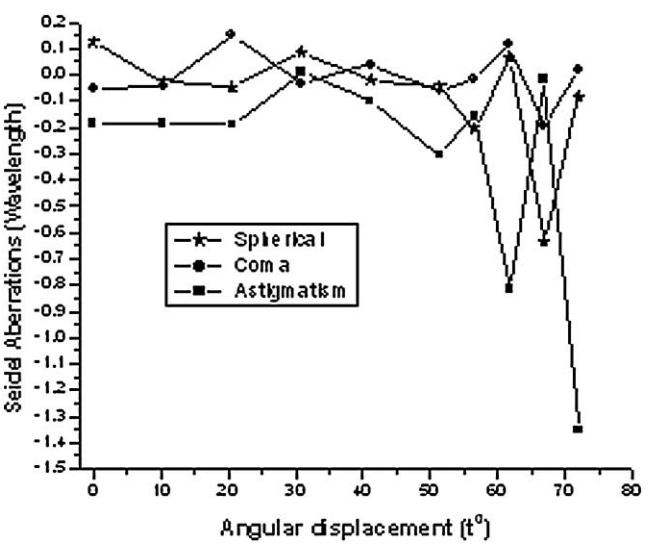


**Fig. 14** Changes in aberrations with angular rotation of the cogwheel.

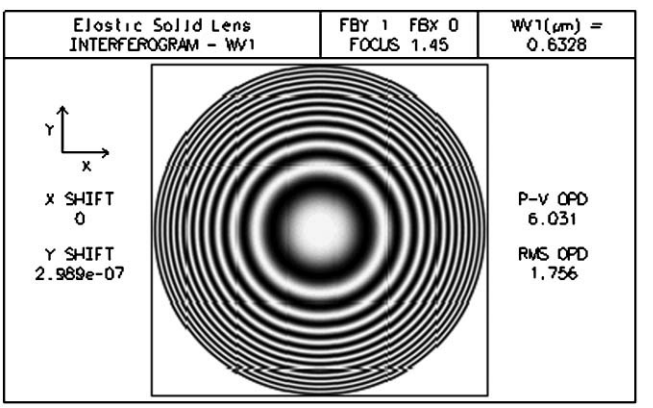


**Fig. 15** Simulated interferogram of SEL with the OSLO™ program.

**Table 3** Aberrations obtained with OSLO from geometrical parameters of the SEL.

| | Zernike Data | PDI within the Focus | 16 Terms |
|---|---|---|---|
| Third-order aberrations in wavelengths | | ($\lambda$= 632.8 nm) | |
| Spherical | 1.96 | Piston | 0 |
| Coma in *Y* | − 0.000017 | Focus | 1.45 |
| Coma in *X* | 0.01 | Tilt in *X* | 0.0 |
| Stigmatism 45 deg | | Tilt in *Y* | 0.0 |
| Stigmatism 0 deg | | | |
| Fifth-order aberrations in waves ($\lambda$ = 632.8 nm) | | | |
| Spherical | 0.5165 | | |
| Coma in *Y* | 0.0 | 0 deg Tri | 0.0 |
| Coma in *X* | 0.0 | 30 deg Tri | 0.0 |
| Stigmatism 45 deg | 0.0 | | |
| Stigmatism 0 deg | 0.0 | | |

## 6 Conclusions

The design and construction of a new solid elastic lens was proposed, this lens being of the tuneable focus type. This design differs radically from those developed so far. It requires only a mechanical mount to apply radial forces at the edge of the lens which is made from a transparent elastic material. Tests showed that the lens has a tunable focus range.

The SEL was characterized by measuring aberrations using the PDI technique, which generates interference patterns (the phase plate was made by the authors at INAOE). The patterns obtained were processed with ApexWin$^{TM}$. Once this program evaluated the patterns, it then produced wavefront aberration values found in the SEL using fifth-order Zernike polynomials. These results in turn enabled us to know the quality of the images formed by the SEL, and on the basis of this, try to correct some of them by modifying the initial shape of the surfaces before the application of forces.

Variations between ideal and experimental results are mainly due to problems in the manufacture of the lens; however, interference patterns obtained in both cases are similar. Finally, the scope of this type of lens is very promising in optical engineering.

### *Acknowledgments*

Our thanks to Consejo Nacional de Ciencia y Tecnologia (CONACYT) for support in carrying out this study through the project entitled Adaptive Optics for Refractor Systems, with registration number SEP2004C01-46080, and CONACYT project P49699-F. Our thanks also to Neil Bruce (Centro de Ciencias Aplicadas y Desarollo Tecnológico, Universidad Nacional Autónoma de México, neil.bruce@ccadet.unam.mx) and Patrick Raferrty (King Fahd University of Petroleum and Minerals, Saudi Arabia, rpatrick@fupm.edu.sa) for revising the manuscript.

### *References*

1. X. Cheng, Y. Wang, Q. Hao, and J. M. Sasian, "Expert system for generating initial layouts of zoom systems with multiple moving lens groups," *Opt. Eng.*, **34**, (1), 013001 (2005).
2. R. Navarro, F. Palos, and L. González, "Adaptive model of the gradient index of the human lens. I. Formulation and model of aging ex vivo lenses," *J. Opt. Soc. Am. A* **24**, 2175–2185 (2007).
3. G. C. Knollman, J. L. S. Bellin, and J. L. Weaver, "Variable-focus liquid-filled hydroacoustic lens," *J. Acoust. Soc. Am.* **49**, 253–261 (1970).
4. A. Santiago-Alvarado, S. Vázquez-Montiel, J. González-García, V. M. García-Luna, A. Fernández-Moreno, and E. Vera-Díaz, "Analysis and design of an adaptive lens," *Proc. SPIE* **6288**, 62880S 1–10 (2006).
5. H. T. Dai, Y. J. Liu, X. W. Sun, and D. Luo,"A negative-positive tunable liquid-crystal microlens array by printing," *Opt. Express* **17**, 4317–4323 (2009).
6. M. M. Peter, D. Saman, H. K. Aik, W. T. Kok, L. C. Mei, and R. Isabel, "Fluidic lenses with variable focal length," *Appl. Phys. Lett.* **88**, 041120 (2006).
7. G.-H. Feng and Y. C. Chou, "Flexible meniscus/biconvex lens system with fluidic-controlled tunable focus applications," *Appl. Opt.* **48**(18), 3284–3290 (2009).
8. S. W. Lee and S. S. Lee, "Focal tunable liquid lens integrated with an electromagnetic actuator," *Appl. Phys. Lett.* **90**, 121129 (2007).
9. H. W. Ren and S. T. Wu, "Variable-focus liquid lens," *Opt. Express* **15**, 5931–5936 (2007).
10. A. Santiago Alvarado, S. Vázquez Montiel, J. González García, B. I. G Licona-Moran, J. A. RayasÁ lvarez, and G. Castro-González, "Fabricación y caracterización de membranas elásticas de PDMS para lentes liquidas con longitud focal variable (LLLFV)," *Ópt. Pura Apl.*, **41**(4), 381–388 (2008), www.sepoptica.es.
11. A. Santiago-Alvarado, S. Vazquez-Montiel, J. Munoz-Lopez, J. Castro-Ramos, and J. A. Delgado-Atencio, "Parametric and scattering characterization of PDMS membranes for optical applications," *Proc. SPIE* **7426**, 742615 (2009).
12. http://pibeta.web.psi.ch/handbook/suppliers/sylgard.pdf. Consulted November 23, 2009.
13. A. Santiago–Alvarado, S. Vázquez–Montiel, F. Iturbide–Jiménez, R. Arriaga–Martínez, and J. González–García, "The design, construction and characterization of a solid elastic lens," in *Current Developments in Lens Design and Optical Engineering IX*, P. Z. Mouroulis, W. J. Smith, and R. B. Johnson, Eds., Proc. SPIE **7060-41**, 1–12 (2008).
14. C. Koliopoulos, O. Kwon, R. Shagam, and J. C. Wyant, "Infrared point-diffraction interferometer," *Opt. Lett.*, **3**, 118–120 (1978).
15. W. P. Linnik, "A simple interferometer for the investigation of optical systems," *C. R. Acad. Sci. URSS*, **5**, 210 (1933) (in Russian).

16. Q. Gong and J. M. Geary, "Modeling point diffraction interferometers," *Opt. Eng.* **35**, (2), 351–356 (1996).
17. E. R. Soriano, P. C. García Flores, F. S. Granados Agustín, and A. C. Rodríguez, "Caracterización de interferómetro por difracción de punto (IDP) con apertura cuasicircular," in *Proc. L Congreso Nacional de Física CNF, Reunión Anual de Óptica RAO*, 1–6 (2007).
18. R. N. Smartt and J. Strong, "Point-diffraction interferometer," *J. Opt. Soc. Am.*, **62**, 737 (1972) (Only abstract).
19. D. Malacara, *Optical Shop Testing*, 3rd ed., pp. 116–117, Wiley, New York, (2007).
20. A. Santiago Alvarado, F. S. Granados Agustín, S. Vázquez Montiel, M. Campos, García, and R. Díaz Uribe, "Characterization of deformable elastic lenses using PDI and null screen," *Proc. SPIE* **7389**, 738935 (2009).
21. R. Arriaga Martínez, "Diseño y construcción de un modelo opto/mecánico del ojo humano utilizando una lente adaptativa," Tesis de Licenciatura, Universidad Tecnológica de la Mixteca, pp. 57–76 (Dec. 2008); http://jupiter.utm.mx/˜tesis_dig/10721.pdf.
22. OSLO Ltd., "Sinclair Optics," version 6.01, Fairport, New York (2001).
23. Lambda Research Corporation, Apex Interferogram Analysis Software User´s Manual, Version 3.0 (2000). http://www.lambdares.com/ Consulted July 17, 2010.
24. D. Malacara, *Optical Shop Testing*, pp. 479–483, Wiley, New York (1979).

**Agustin Santiago-Alvarado** has been a research professor since 1998 with the Mixteca Technological University. He received his physics degree in 1993 from the Puebla Autonomous University (BUAP), México, and his MS and PhD degrees in optics in 1995 and 2001, respectively, both from the National Institute of Astrophysics, Optics and Electronics (INAOE). He is a member of the national system of researchers, México. His research interests include optical testing and optical design.

**Sergio Vázquez-Montiel** earned his physics degree in 1984 from Puebla Autonomous University, México, and his MS degree in optics in 1991 and his PhD degree in 1996, both from the National Institute of Astrophysics, Optics and Electronics, México. He is currently a senior researcher in the Optics Department at the National Institute of Astrophysics, Optics and Electronics. His research interests include biomedical optics, optical testing, and optical design.

**Fermín-Salomón Granados-Agustín** is a researcher with the Optics Department of the National Institute of Astrophysics, Optics, and Electronics (INAOE), México. He recieved his BS degree in physics from the National University of Mexico (UNAM) in 1993 and his MS and PhD degrees in optics in 1995 and 1998, respectively, both from the INAOE. He is a member of the national system of researchers, México. He held a postdoctoral position at the Mirror Lab of the Steward Observatory at the University of Arizona in 1999. He has headed the optical shop at the INAOE since 2005. His research interests include optical information, interferometric optical testing, and instrumentation.

Biographies and photographs of the other authors not available.